Materials
Horizons

ROYAL SOCIETY
OF CHEMISTRY

COMMUNICATION

View Article Online
View Journal | View Issue

Check for updates

Cite this: *Mater. Horiz.*, 2026, 13, 3917

Received 16th December 2025,
Accepted 27th January 2026

DOI: 10.1039/d5mh02403j

rsc.li/materials-horizons

Designing dual-center redox-active π-systems with an ultra-low bandgap for enhanced capacitive deionization desalination

Hao Zhou,[a] Jun Yang,*[a] Yuxi Huang,[a] Kouhua Li,[a] Chuanyan Li,[a] Minjie Shi[a] and Edison Huixiang Ang*[b]

Organic molecules are increasingly explored as electrodes for capacitive deionization (CDI), but their poor electron transport and limited active sites hinder ion diffusion and electrosorption. Here, we report the design of a novel organic electrode, PIND, a quinone–amine fused small molecule featuring a highly conjugated backbone with dual redox-active centers and an ultra-narrow HOMO–LUMO gap of 1.17 eV. The reduced bandgap accelerates electron transfer and redox activation, enabling efficient pseudocapacitive uptake of four Na^+ ions. Density functional theory (DFT) calculations reveal strong Na^+ binding with adsorption energies of −1.04 eV (Na^+) and −1.15 eV ($Na^+{\cdot}H_2O$), indicating facile desolvation and coordination at the active sites. *In situ* measurements and DFT confirm reversible redox activity at the C═O and C═N sites. Electrochemically, PIND electrodes exhibit high pseudocapacitance (~208 F g^{-1}), rapid kinetics, and excellent cycling stability (~96.3% retention after 100 cycles). When integrated into a hybrid CDI device (PIND‖AC), the material achieves high salt adsorption (~89 mg g^{-1} at 1.4 V), fast removal (~2.98 mg g^{-1} min^{-1}), and robust regeneration. These results demonstrate that bandgap-engineered, dual-center organic electrodes like PIND provide a practical route to high-efficiency, reversible electrochemical desalination.

New concepts

Capacitive deionization (CDI) electrodes are typically limited by a trade-off between charge transport kinetics and ion-selectivity. We overcome this by introducing an electronic-structure/active-site co-design concept for molecular electrodes, fusing quinone and amine units into a rigid π-conjugated framework. This creates dual redox-active centers (C═O and C═N) and achieves an ultra-narrow bandgap (1.17 eV), which synergistically enables rapid charge transfer and reversible, multi-ion pseudocapacitive storage (up to 4 Na^+ per unit). When fabricated into a hybrid CDI cell, this design delivers exceptional performance: high capacity (89 mg g^{-1}), fast kinetics, outstanding cycling stability (96% retention over 100 cycles), and significant energy recovery (40.1%). This work establishes bandgap-engineered dual-center π-systems as a versatile blueprint for efficient and sustainable desalination.

1. Introduction

As the global water crisis intensifies, driven by rapid agricultural, industrial, and urban expansion, efficient extraction of freshwater from seawater, brine, and wastewater has become a critical challenge.[1] Conventional desalination technologies, such as multi-stage flash (MSF) and reverse osmosis (RO), dominate industrial applications.[2] MSF relies on multi-stage evaporation under reduced pressure, while RO uses semi-permeable membranes to overcome osmotic pressure gradients. Despite their widespread use, these methods face significant limitations, including high energy and chemical consumption, complex operation, large capital investment, and potential secondary pollution.[3–8]

Capacitive deionization (CDI) has emerged as a promising alternative due to its low energy consumption, environmental friendliness, and operational simplicity.[3,9,10] CDI removes ions *via* charge adsorption or redox reactions at electrode surfaces, making it particularly suitable for low-salinity water treatment.[3,11–13] Compared to traditional methods, CDI offers higher thermodynamic efficiency, lower capital and operational costs, improved water recovery, and tunable output salinity.[3,11] However, the overall performance of CDI is strongly constrained by electrode material limitations, such as low charge efficiency, co-ion repulsion effects, and limited ion adsorption capacity.[14] Traditional carbon-based electrodes, including activated carbon, carbon nanotubes, and graphene, provide high conductivity and large surface area but still deliver modest salt adsorption capacities (SAC ≈ 15–20 mg g^{-1}), limiting desalination efficiency.[2,15,16]

To overcome these challenges, organic small molecules have recently gained attention as CDI electrodes.[17,18] Compared to

---

[a] *School of Materials Science and Engineering, Jiangsu University of Science and Technology, Jiangsu, 212003, P. R. China. E-mail: iamjyang@just.edu.cn*
[b] *Natural Sciences and Science Education, National Institute of Education, Nanyang Technological University, Singapore, 637616, Singapore. E-mail: edison.ang@nie.edu.sg*

carbon-based materials, organic molecules offer abundant functional groups and tunable structures, enabling precise control over charge density, hydrophilicity, and electronegativity, which enhances interactions with salt ions, especially Na^+ ions.[19] Recent studies have demonstrated that introducing hydrophilic groups like –OH into organic small-molecule electrodes can significantly enhance charge efficiency, reduce co-ion exclusion effects, and improve ion adsorption capacity.[20,21] Moreover, the intrinsic redox activity of many organic small molecules enables ion removal through diverse ion-exchange pathways, enriching the adsorption/desorption mechanisms available for CDI and ultimately improving electrochemical stability and desalination performance.[17,22,23] Although the use of organic small molecules in CDI electrodes has shown promising initial progress, existing research remains largely focused on molecular design and performance tuning. Future work must further optimize the electrode microenvironment, including pore structure, functional groups, and charge distribution, to improve ion adsorption kinetics, desalination capacity, and cycling stability.[24–26] Despite advances in incorporating carbon materials to enhance conductivity, many organic electrodes still possess relatively large bandgaps, limiting their electronic conductivity. For example, molecules such as BBL (2.91 eV), TNL (2.94 eV), and DQDPD (3.61 eV) exhibit excellent electrochemical stability but suffer from restricted charge transport due to their wide bandgaps. In addition, many organic electrode materials face challenges arising from unevenly distributed active sites, which constrain their charge-storage capacity. Compounds such as benzothiophene derivatives and nitrogen-doped aromatic molecules (*e.g.*, pyrrole and thiophene) display attractive electrochemical properties,[27] yet their performance is often hampered by limited active-site density. For benzothiophene derivatives in particular, interactions with Na^+ are significantly hindered by the ion's large hydration shell, which slows desolvation and reduces charge-transfer efficiency.[28] Addressing these limitations requires concurrent optimization of the molecular electronic structure and the distribution of active sites to facilitate improved ion diffusion and adsorption, thereby enhancing CDI performance for practical applications. Hybrid capacitive deionization (HCDI), which integrates a faradaic electrode with a capacitive counter-electrode, is a well-established CDI configuration that enables enhanced salt removal and efficient electrochemical regeneration. In this work, an asymmetric PIND‖AC HCDI cell is employed as a representative testbed to elucidate how molecular-level electronic-structure and active-site engineering govern desalination kinetics, salt-removal capacity, and energy recovery. Accordingly, the discussion focuses on the molecular design of PIND rather than on cell-architecture innovation.

In this study, we introduce a novel organic electrode material—PIND—synthesized through a simple hydrothermal reaction between 1,4,5,8-naphthalene tetracarboxylic dianhydride (NTCDA) and 2,3-diaminonaphthalene (2,3-DAN). PIND possesses a unique molecular structure that delivers excellent electrochemical desalination performance. Its C═N (imine) and C═O (carbonyl) groups act as multi-electron redox centers, enabling efficient pseudo-capacitive Na^+ capture. Unlike previously reported small-molecule organic CDI electrodes, which typically enhance performance through functional-group tuning but remain constrained by wide bandgaps and/or single redox motifs, PIND uniquely combines bandgap engineering with dual redox centers (C═O/C═N) within a rigid π-system, enabling rapid charge transfer alongside reversible multi-ion pseudocapacitive Na^+ storage. Additionally, the rigid conjugated backbone and ultra-narrow HOMO–LUMO gap (1.17 eV) endow PIND with high charge-carrier mobility and exceptional electrochemical stability. The significant improvement in the electronic properties of PIND can be attributed to three key structural advantages: (1) narrowed bandgap: the monomers NTCDA (3.66 eV) and 2,3-DAN (4.47 eV), which are quinone- and amine-based materials, respectively, undergo strong electronic interaction when combined. This interaction dramatically reduces the bandgap, resulting in an ultra-narrow HOMO–LUMO gap of 1.17 eV that enables rapid charge-carrier mobility. (2) Quinone–amine structure: PIND adopts a quinone–amine configuration that integrates the stability and redox activity of quinone units with the electron-donating properties of amine groups, thereby improving both electrical conductivity and electrochemical stability. (3) Rigid conjugated backbone: the rigid and fully conjugated backbone promotes efficient π–π stacking, facilitating faster charge transport and enhancing structural robustness. With these combined structural features, PIND demonstrates significantly improved charge mobility, stability, and overall electrochemical efficiency compared with its monomeric precursors. As an electrode material, PIND delivers a highly efficient capacitive response toward Na^+ ions, achieving a specific capacitance of 193 F g^{-1} in aqueous NaCl solution. Building on this advantage, a hybrid capacitive deionization (HCDI) device was constructed using PIND as the anode and AC as the cathode. At a flow rate of 10 mL min^{-1} and an initial NaCl concentration of 500 mg L^{-1}, the optimized device delivered a Na^+ adsorption capacity of 89 mg g^{-1} and an average salt adsorption rate (ASAR) of 2.98 mg g^{-1} min^{-1} under an applied voltage of 1.4 V (t_{ads} = 30 min). The device retained 96.8% of its initial capacity after 200 cycles, demonstrating excellent long-term durability and underscoring its strong potential for sustainable brackish-water treatment, while providing a solid foundation for future extension toward higher-salinity feeds. The exceptional performance of the HCDI device is supported by several factors. The adsorption of Na^+ and hydrated Na^+ plays a central role, with adsorption energies of −1.04 eV and −1.15 eV, respectively. The more favorable adsorption of hydrated Na^+ promotes stronger interaction with active sites on the electrode. In this study, the distribution of functional groups within the electrodes was optimized to accelerate both adsorption and desolvation of hydrated Na^+, thereby enhancing ion transport and improving overall energy efficiency. In addition, the electrode materials possess excellent mechanical strength and chemical stability, which prevents structural collapse or phase transitions and ensures long-term operational stability.

2. Results and discussion

The PIND organic small molecule was synthesized through a dehydration condensation reaction between NTCDA and 2,3-DAN (Fig. S1), yielding the product morphology shown in Fig. S2. This reaction forms an extended conjugated backbone featuring C=O and C=N linkages. The powder Raman spectrum (Fig. S3) exhibits characteristic vibrational bands at approximately 1384 cm^{-1} (C=C/C–C), 1593 cm^{-1} (C=N), and 1614 cm^{-1} (C=O), confirming the presence of aromatic units and a highly conjugated structure. These structural features provide a stable electronic framework capable of supporting ion storage and efficient charge transfer. The high-resolution C 1s XPS spectrum (Fig. 1b) further supports the successful formation of PIND. The spectrum can be deconvoluted into five components corresponding to C=C (284.8 eV), C–C (285.1 eV), C=N (286.3 eV), C=O (288.5 eV), and π–π interactions (290.7 eV). The distinct chemical shifts associated with C=N and C=O provide direct evidence of the functional groups introduced during condensation, while the π–π signal at 290.7 eV indicates strong aromatic stacking interactions between molecular units. Complementary ^1H liquid-phase NMR analysis (Fig. 1c) displays well-resolved chemical shifts and integral distributions, confirming the atomic-level chemical environment and high selectivity of the synthetic process. Morphological characterization reveals that, unlike the disordered precursor powders, PIND forms macro-sized particles with diameters of approximately 2–4 μm. Scanning electron microscopy (SEM) images (Fig. S4) reveal relatively uniform surfaces with locally ordered regions within the bulk. Powder X-ray diffraction (XRD) patterns (Fig. 1d and Fig. S5) show sharp diffraction peaks for the crystalline precursors, whereas PIND displays a broad peak centered at $2\theta \approx 27^\circ$. This broad feature suggests macroscopic amorphous or quasi-amorphous packing, while still preserving π–π stacking of planar aromatic units at the molecular level, consistent with

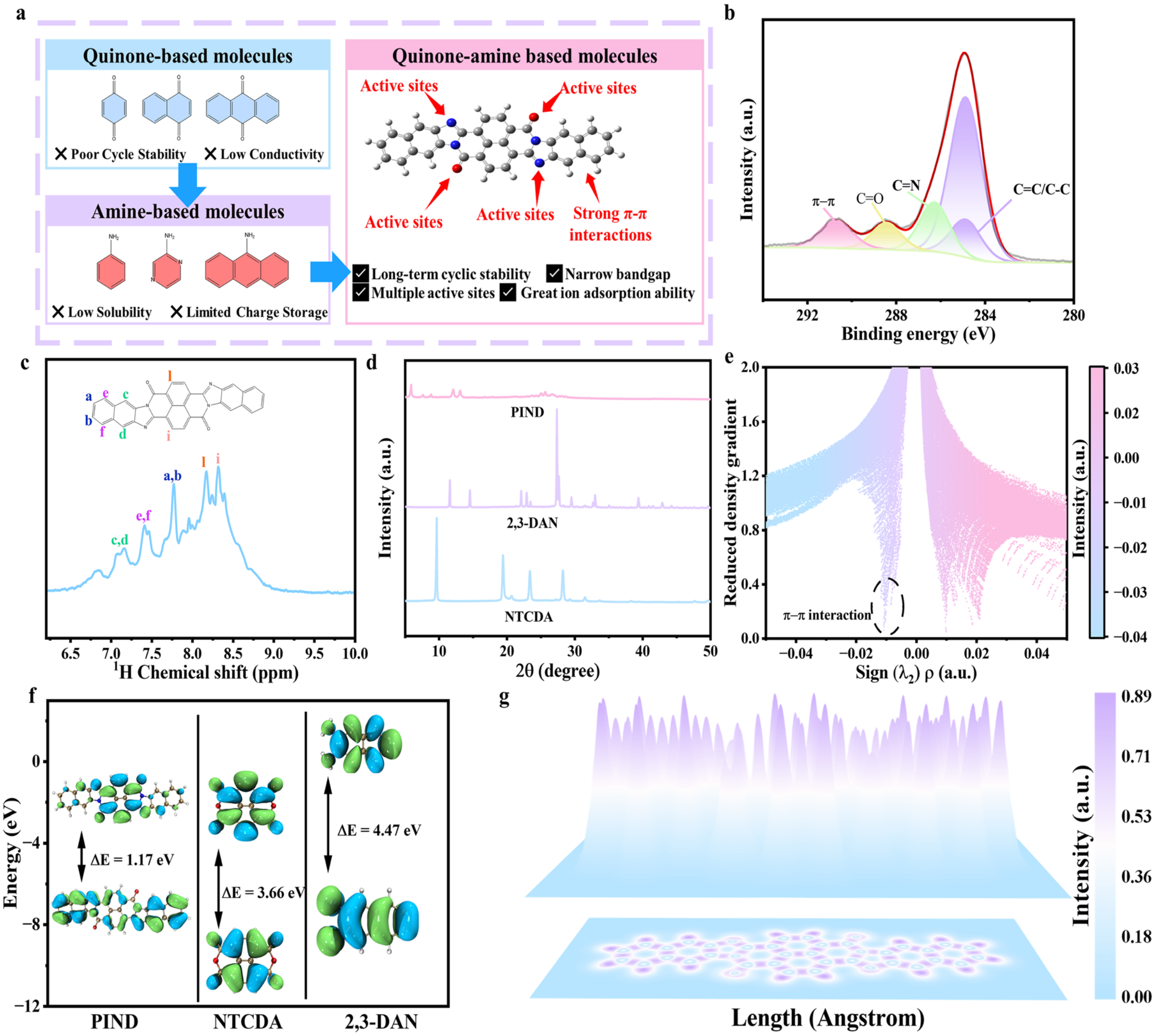

Fig. 1 (a) Structural evolution and active sites of quinone-based, amine-based, and quinone–amine-based molecules. (b) XPS C 1s spectra, (c) ^1H NMR spectrum, (d) XRD pattern, (e) RDG plot of the PIND molecule, (f) HOMO–LUMO calculation of PIND and its corresponding precursors, and (g) LOL–π color-filled map of the PIND molecule.

typical interlayer spacing.[29] As shown in Fig. 1e, the presence of pinkish-purple spikes in the −0.02 to 0.00 a.u. range of sign(λ_2)ρ indicates significant π–π interactions between adjacent molecular chains, which contribute to the structural integrity and overall stability of PIND. Density functional theory (DFT) calculations (Fig. 1f) reveal a substantial narrowing of the HOMO–LUMO gap to 1.17 eV, far smaller than the gaps of the precursors and most conventional electroactive small molecules (>3.0 eV).[30] This reduction reflects the extended π-conjugation and reorganization of molecular orbitals, lowering the activation energy for charge migration and facilitating electron and hole transport. These electronic features underpin the enhanced redox activity and strong electrochemical response observed experimentally.[31] The partial density of states (PDOS, Fig. S5) shows pronounced orbital hybridization near the Fermi level, dominated by C, N, and O p-orbitals. Such hybridization enhances electronic coupling within the conjugated backbone and promotes transitions between valence and conduction states, thereby improving charge-transport properties. The continuous, high-density electronic states near the Fermi level are consistent with a narrow-bandgap material capable of efficient charge excitation and migration. These PDOS results provide strong theoretical support for the fast charge transfer and enhanced redox behavior of PIND electrodes. Localized orbital locator (LOL) analysis (Fig. 1g) shows high LOL values (0.61–0.89) across the backbone, exceeding the 0.53 threshold for electron delocalization in most regions. This confirms extensive π-electron delocalization and a highly conjugated molecular configuration.[32] Taken together, the XPS, NMR, and DFT results, including PDOS and LOL analyses, provide a coherent set of structural and electronic evidence linking the molecular architecture of PIND to its outstanding electronic properties.

To further examine the electrochemical behavior of the PIND molecule, systematic measurements were conducted in NaCl electrolyte using a conventional three-electrode configuration. In this setup, PIND was used as the working electrode, a graphite rod as the counter electrode, and a saturated Ag/AgCl electrode as the reference. Cyclic voltammetry (CV) was performed within a potential window of −1.0 to 0.8 V at scan rates ranging from 1 to 10 mV s^{-1} (Fig. 2a). The CV curves exhibit characteristic pseudocapacitive behavior, displaying distinct anodic peaks at −0.76 V and −0.37 V and cathodic peaks at −0.76 V and −0.56 V, corresponding to the reversible oxidation and reduction processes. These well-defined redox features indicate the presence of abundant and accessible active sites on the PIND electrode, enabling efficient Na$^+$ capture. For comparison, the CV curve of NTCDA (Fig. S6) within −0.6 to 0.3 V shows weak and asymmetric redox peaks with low peak currents and minimal variation across scan rates, indicating sluggish electron-transfer kinetics and diffusion-limited faradaic processes. Meanwhile, the CV curve of 2,3-DAN displays an almost rectangular profile with only slight redox perturbations, characteristic of a predominantly capacitive response lacking pronounced reversible redox activity. As the scan rate increased, the CV curves of the PIND electrode maintained their overall shape, while the peak currents increased proportionally, indicating a stable electrochemical response and efficient faradaic reaction kinetics. The oxidation peaks exhibited only slight shifts from −0.76 V to −0.73 V and from 0.38 V to 0.40 V, while the reduction peaks shifted marginally from −0.564 V to −0.565 V and from −0.76 V to −0.79 V (Fig. 2b). These small variations suggest minimal polarization during charge–discharge processes and confirm the favorable charge-transfer dynamics of the PIND electrode for Na$^+$ storage.[33] To gain deeper insight into the reaction mechanism, the relationship between peak current (i) and scan rate (v) was analyzed using the equation: $i = av^b$, where the b-value provides information on the charge-storage process.[34,35] For the b-value analysis, the peak currents were extracted after baseline correction by subtracting the non-faradaic background current adjacent to each redox peak, and the same procedure was consistently applied across all scan rates. As shown in Fig. 2c, the b-values for the oxidation process were 0.99 and 0.99, while those for the reduction process were 0.71 and 0.65. These values indicate that the PIND electrode exhibits a mixed charge-storage mechanism that includes both strong pseudocapacitive contributions and diffusion-controlled processes.[34] Quantitative separation of capacitive and diffusion-controlled currents (Fig. 2d) revealed pseudocapacitive contributions of 49%, 61%, 71%, 75%, and 77% at scan rates of 1, 2, 5, 8, and 10 mV s^{-1}, respectively. The increasing pseudocapacitive fraction at higher scan rates demonstrates that surface-controlled processes dominate under rapid electrochemical conditions. Galvanostatic charge–discharge (GCD) curves collected at current densities of 1–20 A g^{-1} (Fig. 2e) show nearly triangular, plateau-free profiles, consistent with a pseudocapacitive energy-storage mechanism rather than a battery-type reaction pathway.[36,37] As the current density increased, the charge–discharge time decreased, while the curve shape remained symmetric, indicating highly reversible redox behavior even at fast cycling rates. At 1 A g^{-1}, the PIND electrode delivered long charge–discharge times and high specific capacitance, reflecting efficient ion diffusion and effective utilization of electrochemically active sites. Even at 20 A g^{-1}, the electrode retained stable and well-defined responses, demonstrating excellent rate capability and rapid electron-transfer kinetics. Fig. 2f summarizes the rate performance. The PIND electrode delivered a high specific capacitance of 229.3 F g^{-1} at 1 A g^{-1} and retained more than 60% of this value at 20 A g^{-1}, confirming its robust high-rate performance. Cycling stability measurements (Fig. S7) further show that the specific capacitance remained stable as the current density increased and subsequently returned to the initial value. After switching back to 1 A g^{-1}, the electrode recovered more than 95% of its original capacity, and the Coulombic efficiency remained close to 100% throughout. Long-term stability was further evaluated through extended cycling in 1 M NaCl (Fig. 2g). After 20,000 charge–discharge cycles at 5 A g^{-1}, the PIND electrode maintained a capacitance of approximately 70 F g^{-1}, with minimal fluctuation and a Coulombic efficiency consistently between 98 and 100%. In contrast, the precursor monomers NTCDA and 2,3-DAN exhibited poor cycling stability (Fig. S8). Under identical conditions,

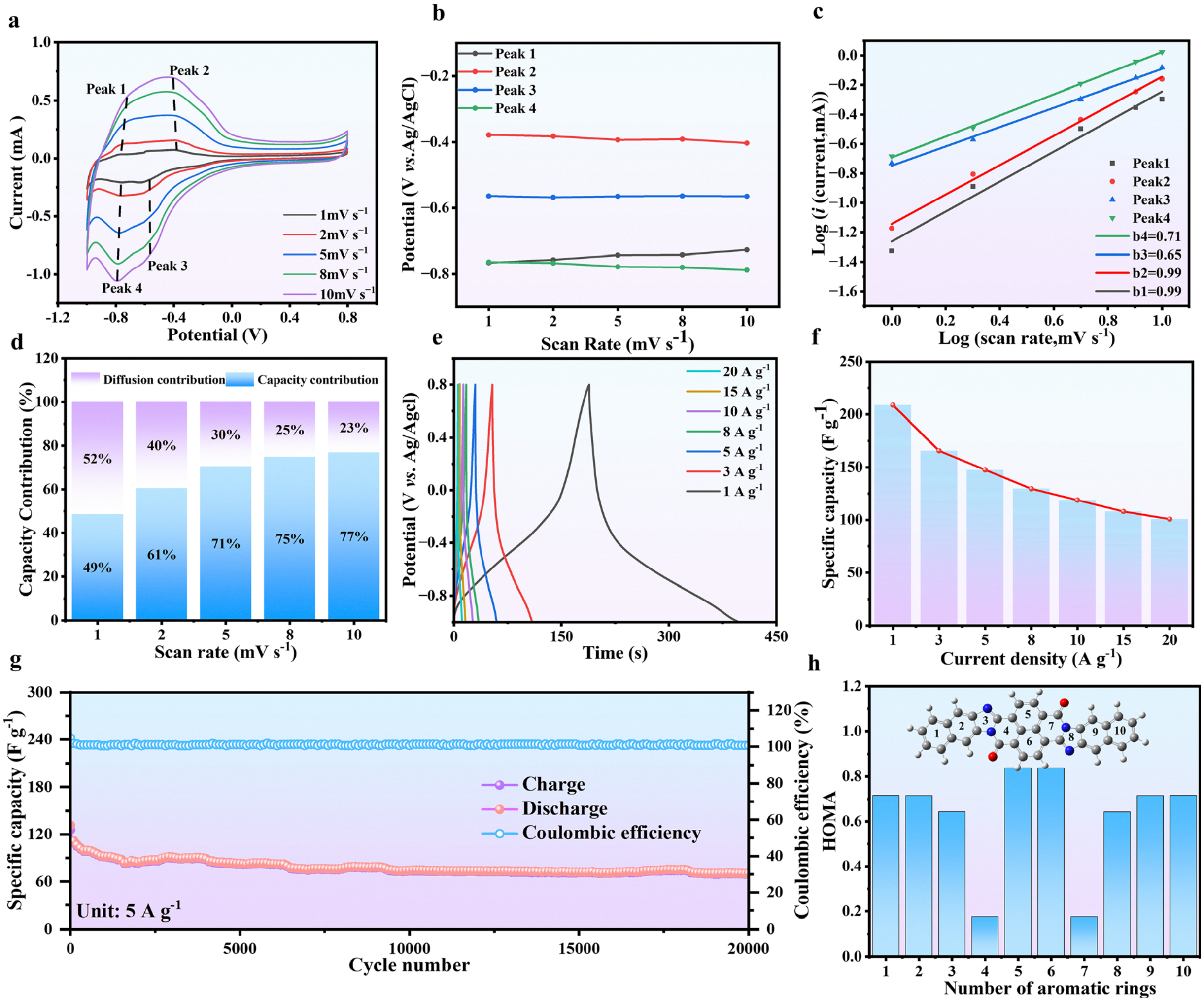

Fig. 2 (a) CV profiles and (b) the corresponding peak potentials at scan rates ranging from 1 to 10 mV s^{-1} in 1 M NaCl aqueous electrolyte and (c) the corresponding *b*-values at various redox peaks, (d) capacitive contribution ratios under various scan rates, (e) GCD curves and (f) the corresponding specific capacitances of the PIND electrode under different densities, (g) long-term cycling stability, and (h) the calculated values for the PIND molecule.

NTCDA retained only 5–10 F g^{-1} with gradual decay, indicating insufficient active sites and limited faradaic reversibility, while 2,3-DAN showed capacitances below 10 F g^{-1} with large fluctuations, reflecting poor structural robustness and weak electrochemical activity. These comparisons highlight the markedly superior electrochemical durability and stability of the PIND electrode. The resonance aromaticity model (HOMA) was used to quantify the aromaticity and backbone stability of PIND before and after Na$^+$ adsorption (Fig. 2h). The PIND molecule exhibited moderate to high aromaticity across most sites (HOMA values of approximately 0.6–1.0), indicating a well-conjugated π-framework. Upon adsorption of 2 or 4 Na$^+$ ions (Fig. S9), HOMA values near N and O atoms increased, approaching 1, suggesting enhanced aromaticity and structural stabilization due to redistribution of electron density.[38] Small decreases at a few sites reflect reversible local perturbations during coordination. Overall, these results show that Na$^+$ adsorption does not disrupt the conjugated backbone but instead enhances electron delocalization and structural rigidity, providing a molecular-level explanation for the outstanding cycling stability and reversible Na$^+$ capture observed in the PIND electrode.

As shown in Fig. 3a, the DRT contour plot displays a prominent peak in the mid-to-low frequency region ($\tau \approx 10^{-1}$–10^{0} s), indicating that diffusion and desorption processes dominate the overall impedance at this time scale. A smaller peak appears in the high-frequency region, corresponding to current collection and particle contact resistance. During charge–discharge cycling, the amplitude of the mid-frequency (charge-transfer) peak rapidly decreases and stabilizes, suggesting that the active sites and interfacial layer become fully activated within the first cycle and subsequently form stable reaction pathways. These observations indicate that the impedance of PIND includes substantial surface pseudocapacitive contributions while maintaining effective ion-diffusion channels at slower time scales, jointly supporting its high capacity and strong rate performance. A linear fit of Z' *versus* $\omega^{-1/2}$ in the low-frequency region (Fig. 3b) yields a strong linear

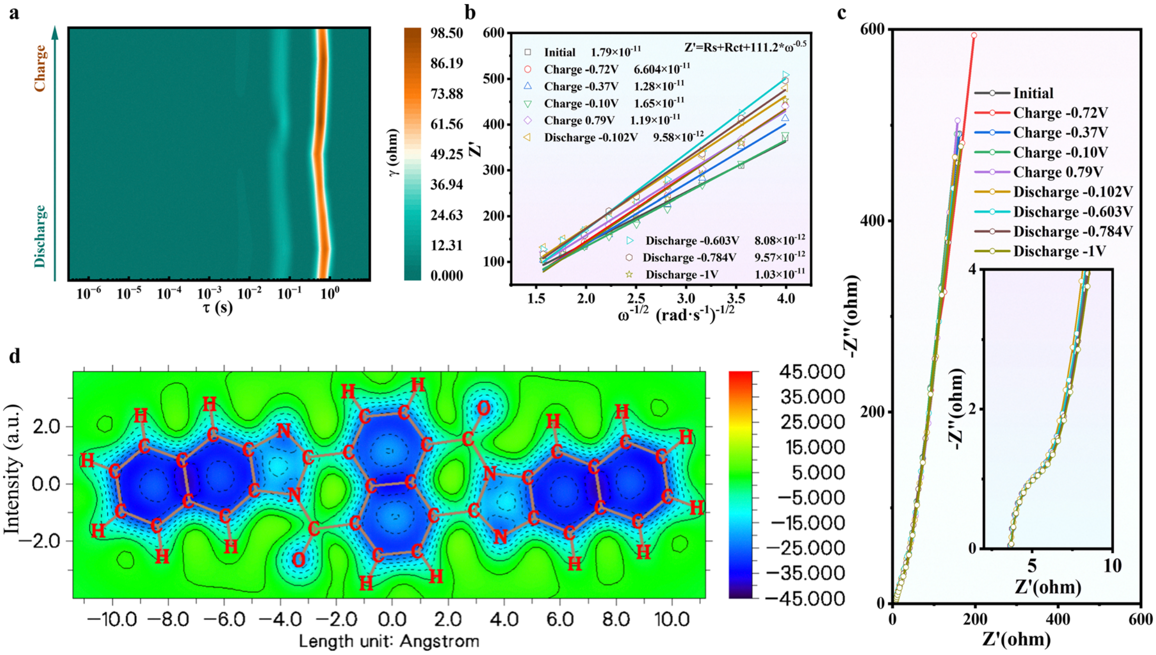

Fig. 3 (a) DRT analysis of the PIND electrode upon charging and discharging. (b) D_{Na^+} coefficients at various states. (c) *Ex situ* EIS plots of the PIND electrode. The inset shows the amplified high-frequency region. (d) NICS-*zz* contour plot mapping the anisotropic magnetic shielding effects across a cross-section perpendicular to the PIND molecule.

relationship. The Na^+ diffusion coefficient D, calculated from the slope of the fit, falls within the range of 1.79×10^{-11} to 1.03×10^{-11} $cm^2\ s^{-1}$, demonstrating rapid ion migration under electrochemical conditions.[39,40] This is consistent with the nearly symmetrical and reversible voltage–time profiles obtained during galvanostatic charge–discharge measurements. The Bode plot (Fig. S10) reveals characteristic phase–angle transitions and a phase minimum across specific frequency bands, marking the shift from electronic/interface charge-transfer processes to ion-diffusion control. The characteristic frequency near 1 Hz represents the rapid response window of pseudocapacitive/faradaic reactions, followed by a slower regime dominated by ion diffusion. The narrow energy gap of the PIND molecule reduces the electron-transport time constant, shifting the frequency features associated with electronic motion to higher frequencies. This appears in the Bode plot as a faster phase response and reduced high-frequency impedance. The Nyquist plot of the PIND electrode (Fig. 3c) exhibits only a very small or nearly invisible semicircle at high frequencies, together with an almost vertical line at low frequencies. This indicates extremely low charge-transfer resistance at the electrode–electrolyte interface and highly reversible ion diffusion. Equivalent-circuit fitting using the R_s–R_{ct}–C_{PE}–Z_w model (Table S1) shows that the charge-transfer resistance R_{ct} remains below 2.5 Ω and stays stable throughout cycling, confirming a robust interface and efficient charge-exchange pathways. A comparison with the two precursor monomers, NTCDA and 2,3-DAN (Fig. S11), shows that PIND exhibits much smaller semicircle diameters and steeper low-frequency slopes, demonstrating superior charge-transfer kinetics and faster ion-diffusion behavior. The enlarged Nyquist plot in the inset further highlights the low interfacial resistance and efficient Na^+ transport channels in PIND, which underpin its high specific capacitance and rapid charge–discharge characteristics. These experimental findings align with the electronic-structure analysis. LOL–π results (Fig. S12) reveal uniform electron-density distribution and extensive π-electron delocalization in PIND during Na^+ adsorption. NICS-*zz* calculations (Fig. 3d) confirm strong aromaticity and enhanced π-conjugation, which promote efficient charge transport and contribute to the exceptional electrochemical properties of the PIND electrode.

To elucidate the mechanisms governing Na^+ storage in PIND electrodes, Raman spectroscopy was performed (Fig. 4a). *In situ* Raman spectra (Fig. 4b) reveal dynamic bond variations during electrochemical cycling. The characteristic C═O band at 1614 cm^{-1} and the C═N band at 1593 cm^{-1} exhibit reversible intensity changes—initially increasing and then decreasing—indicating repeated structural modulation associated with Na^+ insertion and extraction. *Ex situ* Raman measurements (Fig. 4c and d) show similar trends, further confirming that these functional groups are electrochemically accessible and actively participate in the redox processes of PIND during charge–discharge operation. To probe chemical-state evolution at electrochemically active sites, XPS was conducted before and after discharge. The O 1s spectrum shows a peak at 532.1 eV corresponding to carbonyl (C═O) groups (Fig. 4e), confirming the presence of stable carbonyl moieties in the PIND framework. During charging, the C═O signal remains largely unchanged, indicating structural integrity in the oxidized state. Upon discharge, however, the C═O peak decreases and shifts to a C–O peak at ~533.3 eV, demonstrating that carbonyl groups undergo reduction *via* Na^+ interaction to form C–O species.[41,42] This provides direct evidence that carbonyl groups

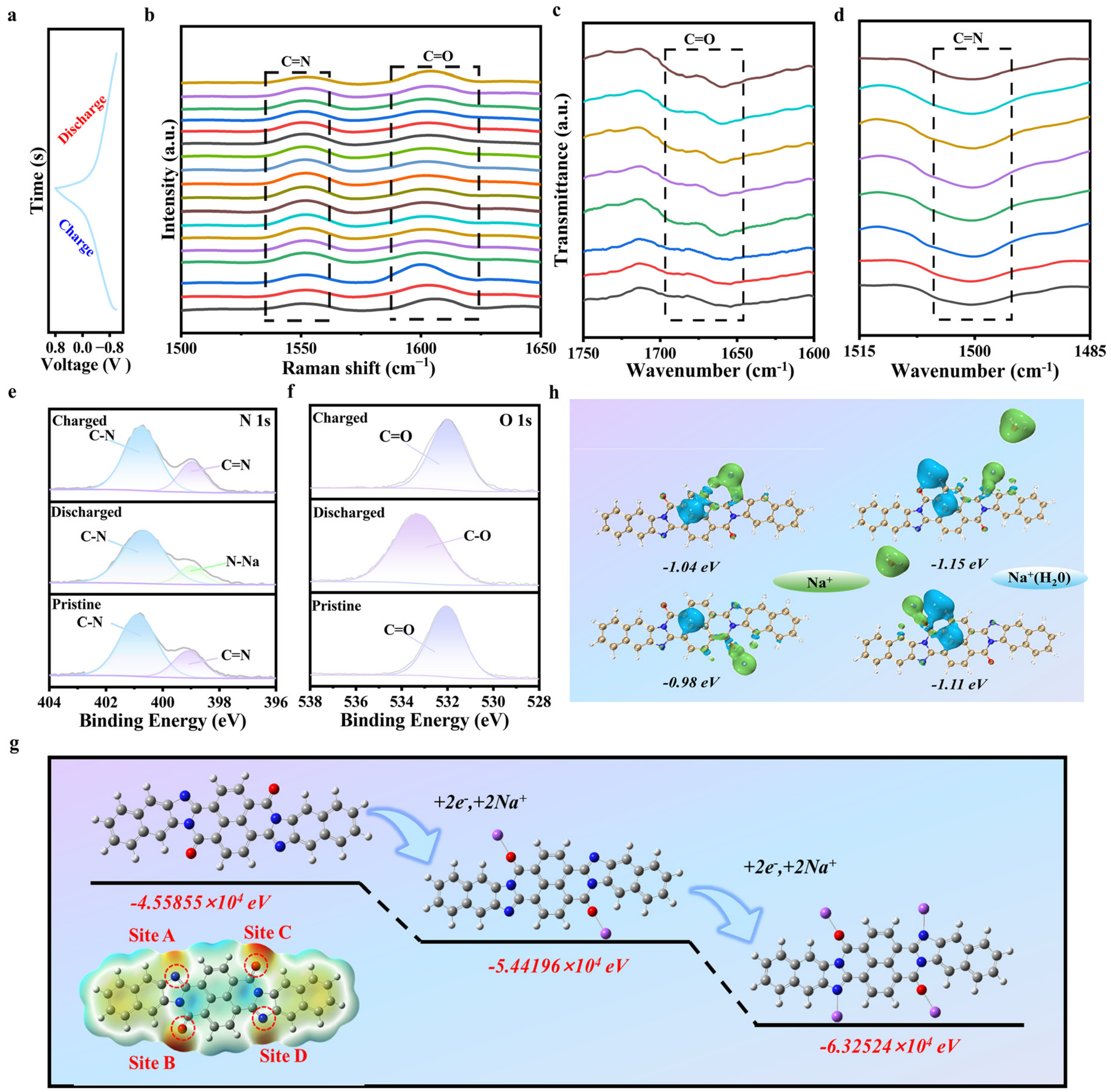

Fig. 4 (a) GCD curves of the PIND electrode during discharging and charging, (b) the corresponding *in situ* Raman spectra of the PIND electrode and (c) and (d) *ex situ* FTIR spectra of the PIND electrode. (e) N 1s and (f) O 1s spectra of the PIND electrode in *ex situ* XPS spectra under various charging and discharging conditions. (g) The proposed Na^+ adsorption pathway obtained from DFT simulations. (h) Calculated adsorption energies of the PIND electrode towards Na^+ and Na^+ H_2O at different active sites.

act as redox-active centers during sodiation. Similarly, the N 1s spectrum (Fig. 4f) shows significant changes: during discharge, the original imine C═N peak at 398.98 eV disappears, accompanied by the appearance of a new N–Na peak at 399.88 eV. This confirms the coordination of Na^+ with imine nitrogen and highlights the involvement of C═N sites in Na^+ storage. Together, the combined Raman and XPS results demonstrate that both C═O and C═N centers are reversibly engaged during cycling, supporting efficient utilization of the dual redox-active sites under electrosorption/desorption conditions. Based on spectroscopic evidence and DFT analysis, the reversible sodiation/desodiation at these sites can be expressed as:

$$\mathrm{C{=}O + Na^+ + e^- \rightleftharpoons C{-}O{-}Na^+}$$

$$\mathrm{C{=}N + Na^+ + e^- \rightleftharpoons C{=}N{-}Na^+}$$

Accordingly, each PIND unit can reversibly host up to four Na^+ ions through multi-electron transfer:

$$\mathrm{PIND} + x\mathrm{Na^+} + x\mathrm{e^-} \rightleftharpoons \mathrm{Na}_x\mathrm{PIND}\ (x \leq 4)$$

Molecular electrostatic potential (MESP) mapping (Fig. 4g) identifies strongly negative regions around C═O and C═N groups, indicating favorable electrophilic binding sites for Na^+ ions.[43] Electronegativity analysis (Table S2) identifies four reactive sites (A–D) within PIND. Theoretical calculations indicate that Na^+ insertion follows a minimum-energy pathway, with progressively reduced binding energy during discharge, demonstrating that Na^+ adsorption is both stable and reversible. Each structural unit of PIND accommodates up to four Na^+ ions with minimal structural deformation, highlighting the polymer's excellent redox stability.[35] Fig. 4h shows the calculated adsorption energies of Na^+ and hydrated Na^+ at site A, which are −1.04 eV and −1.15 eV, respectively. The slightly stronger adsorption of hydrated Na^+ suggests that solvation enhances the interaction between Na^+ and the PIND framework. Water molecules stabilize Na^+ through solvation, strengthening the overall adsorption of hydrated ions relative to bare Na^+ ions.

To comprehensively evaluate the Na^+ removal performance of the synthesized PIND molecules, batch-mode electrosorption experiments were carried out using an asymmetric HCDI configuration, with PIND as the cathode and AC as the anode (PIND‖AC) (Fig. 5a). A detailed schematic of the two-stage operation of the PIND‖AC HCDI cell, covering electrosorption and polarity-reversal regeneration, is provided in Fig. S16. The schematic on the left illustrates the layered assembly of the device, including the shell, electrodes, and ion-exchange membrane. In this system, PIND selectively adsorbs Na^+ ions at the cathode, while AC captures Cl^- ions at the anode, enabling efficient ion separation. Notably, although AC contributes to ion electrosorption *via* electrical double-layer (EDL) processes, the ion-exchange membrane regulates ion transport and suppresses co-ion effects, thereby directing Na^+ migration toward the PIND cathode and Cl^- toward the AC anode during both electrosorption and polarity-reversal regeneration. This membrane-guided ion transport, combined with faradaic Na^+ storage at the redox-active C═O and C═N centers in PIND, underpins the unique and critical role of PIND in the hybrid device. The central panel highlights the chemical structure of PIND, emphasizing its highly conjugated π-system and the

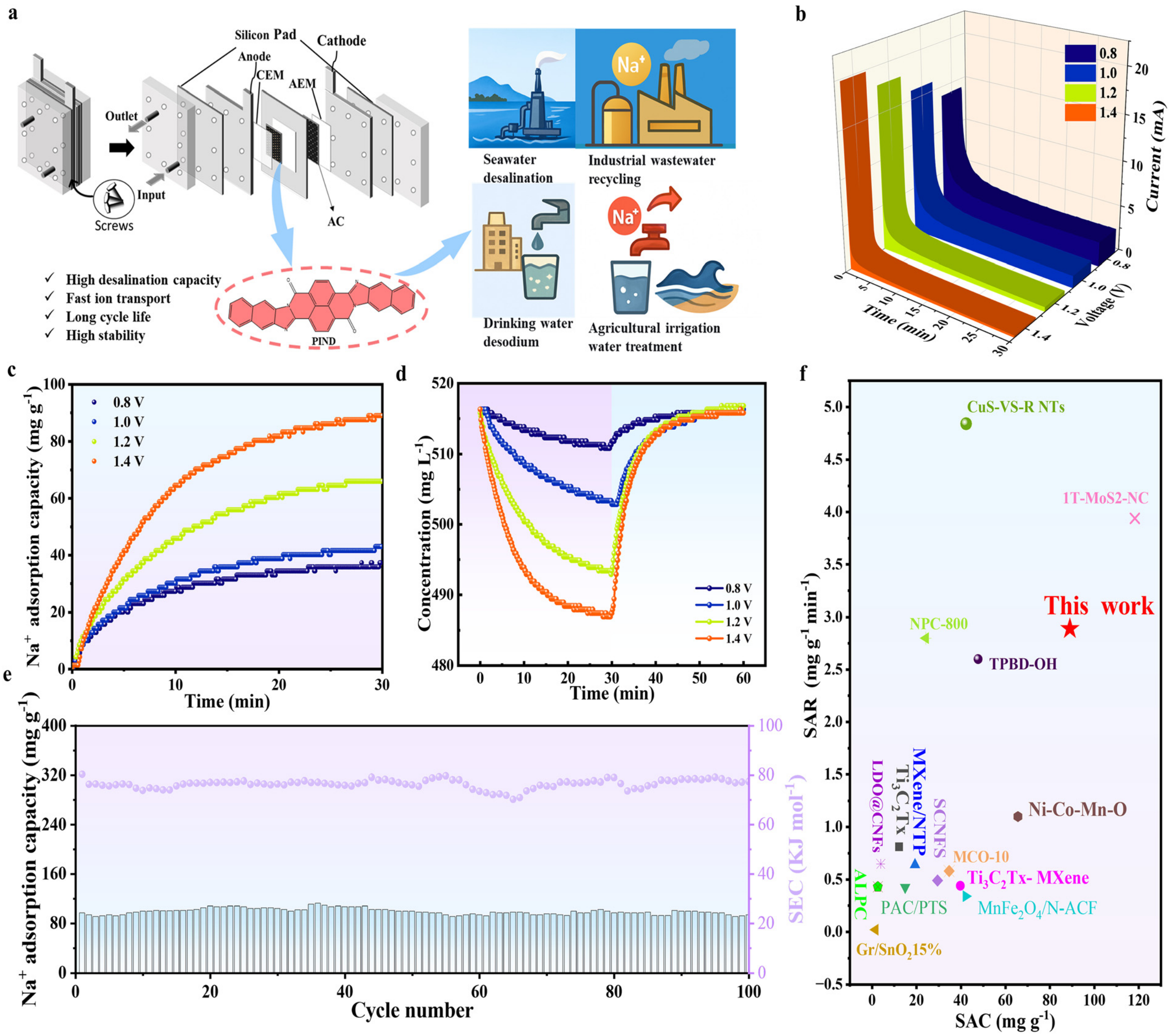

Fig. 5 (a) Schematic of the PIND-based HCDI device and its applications. (b) Current response profiles of the PIND-based CDI device under applied voltages ranging from 0.8 to 1.4 V. (c) Adsorption capacities of the PIND-based CDI device under applied voltages ranging from 0.8 to 1.4 V. (d) The corresponding variations of salt concentration *versus* time. (e) Regeneration stability and the corresponding specific energy consumption (SEC) values over 100 cycles at 1.4 V. (f) Comparison of Na^+ removal performance with previously reported HCDI devices.

presence of C═O and C═N functional groups, which contribute to enhanced charge transfer and ion adsorption. The right panel depicts potential applications of the device, including seawater desalination, industrial water reuse, desodium treatment of drinking water, and agricultural irrigation, highlighting the broad applicability of PIND for sustainable water management. To ensure reproducibility and clarity of the CDI measurements, detailed experimental procedures are provided in Fig. S13. Briefly, HCDI tests were conducted in a two-electrode cell using PIND as the cation-capture electrode and activated carbon (AC) as the counter electrode, separated by an ion-exchange membrane. An aqueous NaCl solution was used as a model brackish feed and operated in batch mode. A constant cell voltage of 1.4 V was applied for 30 min to drive electrosorption, followed by polarity reversal for regeneration. Salt concentration was monitored *via* conductivity and converted to NaCl concentration using a pre-calibrated conductivity–concentration curve. All salt adsorption metrics were calculated from changes in NaCl concentration and normalized to the mass of PIND.

Electrosorption tests were conducted under applied voltages ranging from 0.8 to 1.4 V. Upon application of an external bias, the system exhibited a large instantaneous current that rapidly decayed to a steady-state equilibrium (Fig. 5b). Meanwhile, the solution pH remains nearly constant and close to neutral throughout an adsorption/desorption cycle (∼7.1–7.6; Fig. S18), indicating that parasitic water-splitting reactions are minimal under the applied full-cell voltage. During this process, the PIND electrode facilitated Na^+ transport and adsorption *via* a redox-mediated mechanism, while the AC electrode efficiently captured Cl^- ions due to its high surface area. Increasing the applied voltage enhanced electrostatic attraction, thereby significantly improving ion adsorption capacity. Quantitative analysis revealed that desalination capacities increased from 37.32 mg g^{-1} at 0.8 V to 88.99 mg g^{-1} at 1.4 V (Fig. 5c), demonstrating a strong voltage-dependent performance enhancement. To investigate the effects of salinity, additional Na^+ removal tests were performed in the range of 500–1000 mg L^{-1}, and electrochemical measurements were carried out in the NaCl concentration range of 10 000–30 000 mg L^{-1} (Fig. S19). Fig. 5d further illustrates that both desalination capacity and kinetics improved with increasing voltage, with an average desalination rate of 2.98 mg g^{-1} min^{-1} at 1.4 V. The concentration–time profiles under an initial NaCl concentration of ∼500 mg L^{-1} (Fig. 5d) show rapid initial decreases due to electric-field-driven adsorption, followed by a gradual approach to saturation. Polarity reversal led to a rapid restoration of solution conductivity. Notably, at 1.4 V, the PIND electrode exhibited both rapid Na^+ release and high adsorption rates. Lower voltages resulted in slower ion adsorption (Fig. S14), while the narrow bandgap of PIND (1.17 eV) enables high electronic mobility and rapid charge transfer, ensuring full activation of redox sites and promoting uniform ion diffusion. Consequently, even at moderate voltages, the electrode demonstrates efficient and near-saturation adsorption without a distinct plateau. Long-term cycling tests of the PIND‖AC system at a constant voltage of 1.4 V confirmed its excellent stability and repeatability over 100 cycles (Fig. 5e). The Na^+ removal capacity remained at 96.3% of its initial value, and the solution conductivity exhibited minimal fluctuation, indicating strong regeneration capability. Furthermore, *operando* UV-vis monitoring of the electrolyte during HCDI operation (200–800 nm) revealed no discernible spectral changes or new absorption features compared with the initial electrolyte (Fig. S17), suggesting negligible dissolution or leaching of PIND under the tested aqueous conditions. Overall, the Na^+ removal capacity of this HCDI device significantly exceeds that of previously reported systems (Fig. 5f),[20,44–52] highlighting the outstanding performance and practical potential of PIND for efficient and sustainable water purification.

In addition to achieving high desalination efficiency, the PIND electrode exhibits notable energy recovery capabilities. As shown in Fig. 6a, the system operates in two distinct phases: (1) energy recovery during voltage transitions from ±1.5 V to 0 V (blue shaded region) and (2) energy consumption during the reverse transition from 0 V to ±1.5 V (red region). Fig. 6b further highlights the strong correlation between current density and energy recovery efficiency, showing a pronounced increase in efficiency with increasing current density. Remarkably, the assembled HCDI device achieves an energy recovery efficiency of 40.1% at 4 A g^{-1}, underscoring its potential for sustainable energy applications. In practical systems, harnessing this recoverable energy for net energy savings typically requires bidirectional power-electronics circuitry (*e.g.*, a bidirectional DC–DC converter or a switched-capacitor recovery circuit) coupled with an intermediate storage unit, and some conversion losses are expected. Fig. 6c demonstrates that the PIND electrode exhibits a clear voltage-dependent response across different electrolytes, with preferential Na^+ uptake and appreciable Sr^{2+} adsorption at elevated potentials. This electrolyte-dependent selectivity suggests that PIND is well-suited for selective electrosorption in complex aqueous environments. Complementary adsorption energy calculations (Fig. 6d) support these observations, revealing a significantly more favorable adsorption energy for Na^+ compared with K^+, Mg^{2+}, and Ca^{2+}, indicating a stronger thermodynamic affinity toward Na^+. The consistency between experimental selectivity and computational predictions confirms that PIND offers both kinetic accessibility and an intrinsic energetic preference for Na^+, making it particularly attractive for selective Na^+ capture, storage, and separation under varied electrolyte conditions. To elucidate the adsorption mechanism of Na^+ on the PIND electrode within the HCDI system, kinetic and thermodynamic models were applied to examine the relationship between Na^+ adsorption, desalination time, and initial concentration.[53] The pseudo-second-order model (R^2 = 0.9989) provides a superior fit to the experimental data compared with the pseudo-first-order model (R^2 = 0.9953), indicating that the adsorption process is predominantly governed by field-induced chemical reactions rather than diffusion-limited mechanisms (Fig. S15 and Table S3). Notably, the narrow bandgap of PIND (1.17 eV) facilitates excellent electron transfer and high charge mobility, accelerating redox reaction kinetics and corroborating the

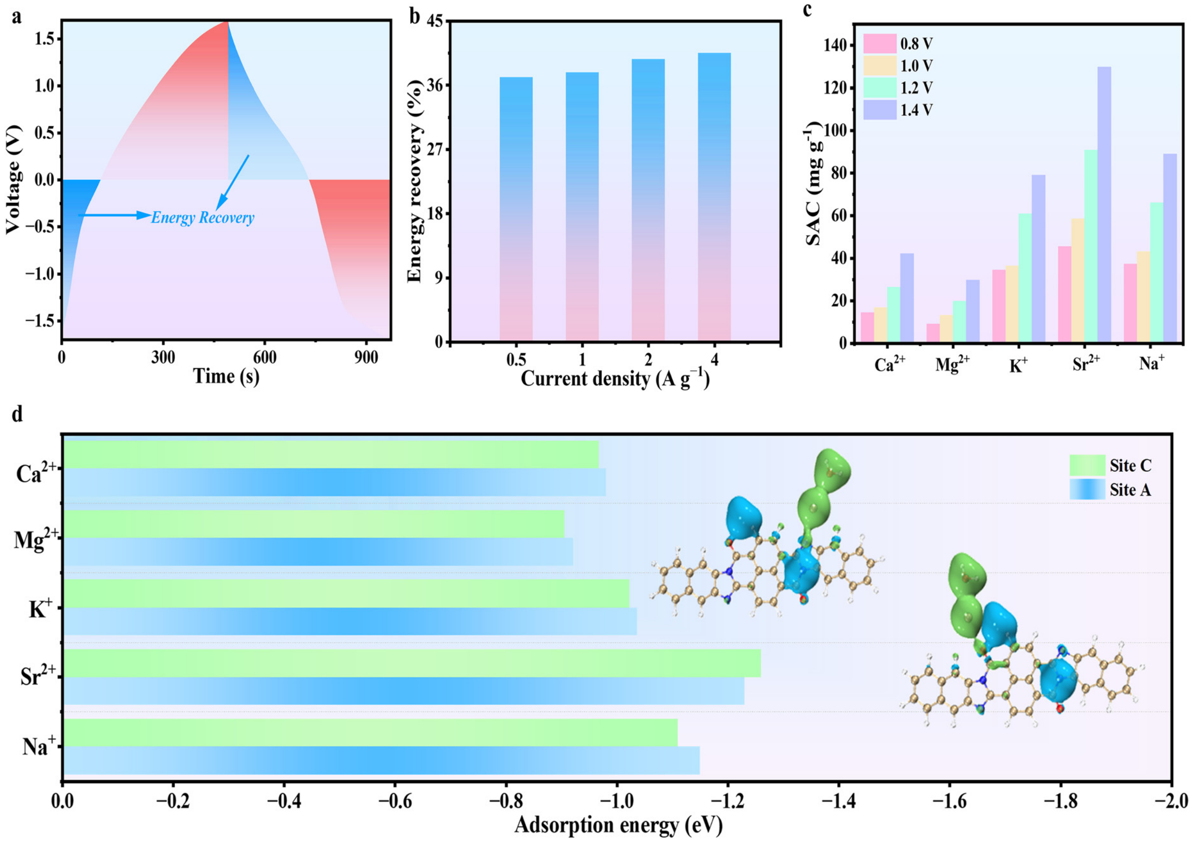

Fig. 6 (a) Real-time voltage variation of the HCDI device during charge/discharge processes. (b) Energy recovery efficiency as a function of applied current density. (c) Salt adsorption capacity (SAC) of different ions at various applied voltages. (d) Adsorption energy of different ions on the PIND electrode.

material's exceptional electrochemical response during rapid Na^+ adsorption.

3. Conclusion

In this study, we report on the development of a novel organic electrode material, PIND, for capacitive deionization (CDI) applications. PIND features an ultra-narrow bandgap of 1.17 eV, which facilitates rapid charge transfer and enhances redox activity, resulting in improved desalination performance. *In situ* characterizations, including XPS and Raman spectroscopy, revealed that the C═N and C═O functional groups of PIND actively coordinate Na^+ ions, with the hydration shell further promoting ion diffusion and desolvation. DFT calculations corroborated these findings, highlighting the critical roles of C═N and C═O sites in the ion adsorption process. Electrochemical measurements demonstrated high capacitance (193 F g^{-1}) and excellent cycling stability, with 96.8% retention after 200 cycles. In CDI tests, PIND achieved outstanding desalination capacity (89 mg g^{-1}) and an energy recovery efficiency of 40.1%. This work underscores the importance of simultaneously optimizing the electronic structure and active sites in organic materials to enhance CDI performance. By integrating *in situ* spectroscopy, DFT simulations, and electrochemical analyses, this study provides fundamental insights into ion diffusion and adsorption mechanisms, paving the way for the design of efficient organic electrodes for sustainable water purification technologies.

Author contributions

J. Yang and E. H. Ang developed the conceptual framework and designed the experiments. J. Yang, H. Zhou and Y. Huang were responsible for material fabrication. H. Zhou and K. Li also performed data measurements, while J. Yang, H. Zhou, and E. H. Ang participated in formal analysis, and H. Zhou performed DFT calculations. H. Zhou and J. Yang conducted data investigation. C. Li and M. Shi handled data analysis. The manuscript was prepared by J. Yang and E. H. Ang. Funding support was provided by C. Li, J. Yang and E. H. Ang. All authors contributed to discussions and provided feedback on the manuscript.

Conflicts of interest

There are no conflicts to declare.

Data availability

The authors confirm that the data supporting the findings of this study are available within the article and/or its supplementary information (SI). Supplementary information of the preparation and testing methods of electrode materials, along with additional characterization of material morphology, structure, electrochemical performance, and CDI performance can be found. See DOI: https://doi.org/10.1039/d5mh02403j.

Detailed data are available from the corresponding author upon reasonable request.

Acknowledgements

We sincerely acknowledge the financial support for this project from the National Natural Science Foundation of China (52402360), China Postdoctoral Science Foundation (2022M7 11686), and the Ministry of Education, Singapore, under its Academic Research Fund (RG88/23).

Notes and references

1 H. Wang, X. Xu, X. Gao, Y. Li, T. Lu and L. Pan, Design of three-dimensional faradaic electrode materials for high-performance capacitive deionization, *Coord. Chem. Rev.*, 2024, **510**, 215835.
2 L. Wang, C. Y. Tang, Y. Hu, B. Chen and W. Xing, Nanofiltration and reverse osmosis technologies for disinfection by-product removal, *Nat. Water*, 2025, **3**, 388–414.
3 C. Zhang, J. Ma, L. Wu, J. Sun, L. Wang, T. Li and T. D. Waite, Flow Electrode Capacitive Deionization (FCDI): Recent Developments, Environmental Applications, and Future Perspectives, *Environ. Sci. Technol.*, 2021, **55**, 4243–4267.
4 M. Son, S. Park, N. Kim, A. T. Angeles, Y. Kim and K. H. Cho, Simultaneous Energy Storage and Seawater Desalination using Rechargeable Seawater Battery: Feasibility and Future Directions, *Adv. Sci.*, 2021, **8**, e2101289.
5 J. Gu, L. Chen, X. Li, G. Luo, L. Fan, Y. Chao, H. Ji and W. Zhu, Multifunctional AlPO4 reconstructed LiMn2O4 surface for electrochemical lithium extraction from brine, *J. Energy Chem.*, 2024, **89**, 410–421.
6 J. Tang, Q. Luo and K. Shi, Fabrication of single-crystal Li-rich manganese oxides as the electrode for electrochemical lithium extraction, *Ceram. Int.*, 2025, **51**, 51526–51534.
7 J. Tang, Q. Luo, Z. Wu and K. Shi, Single-crystalline Al-doped LiMn2O4 nanotubes for electrochemical lithium extraction from brines, *Chem. Eng. J.*, 2025, **505**, 159256.
8 H. Fu, X. Wang, J. Yang, Z. Wu, H. Ren, J. Ji, M. Shi and E. H. Ang, In situ surface manipulation Mn-based Prussian blue analogues with enhanced redox chemistry and ion diffusion toward high-energy-density aqueous sodium-ion batteries, *Chem. Sci.*, 2026, **17**, 968–976.
9 L. Wang, J. E. Dykstra and S. Lin, Energy Efficiency of Capacitive Deionization, *Environ. Sci. Technol.*, 2019, **53**, 3366–3378.
10 K. G. Sun, M. Tebyetekerwa, C. Wang, X. F. Wang, X. W. Zhang and X. S. Zhao, Electrocapacitive Deionization: Mechanisms, Electrodes, and Cell Designs, *Adv. Funct. Mater.*, 2023, **33**, 2213578.
11 Q. Li, Y. Zheng, D. Xiao, T. Or, R. Gao, Z. Li, M. Feng, L. Shui, G. Zhou, X. Wang and Z. Chen, Faradaic Electrodes Open a New Era for Capacitive Deionization, *Adv. Sci.*, 2020, **7**, 2002213.
12 N. E. Mansoor, L. A. Diaz, C. E. Shuck, Y. Gogotsi, T. E. Lister and D. Estrada, Removal and recovery of ammonia from simulated wastewater using Ti3C2Tx MXene in flow electrode capacitive deionization, *npj Clean Water*, 2022, **5**, 26.
13 E. N. Guyes, T. Malka and M. E. Suss, Enhancing the Ion-Size-Based Selectivity of Capacitive Deionization Electrodes, *Environ. Sci. Technol.*, 2019, **53**, 8447–8454.
14 X. Zhao, Y. Zheng, Z. Zheng, Z. Guo, T. Sun, J. Qin, N. Qiu, Z. Zhang and W. Wen, Pre-oxidized ultramicroporous carbon cloth with ultrahigh volumetric capacity and ultralong lifespan for capacitive desalination, *npj Clean Water*, 2023, **6**, 71.
15 R. Cao, J. Zhou, D. Wang, J. Zhang, Y. Zhang, H. Zhou and J. Li, Improving capacitive deionization performance by using O2 plasma modified carbon black, *Chem. Eng. J.*, 2023, **451**, 138530.
16 L. Xu, S. Peng, Y. Mao, Y. Zong, X. Zhang and D. Wu, Enhancing Brackish Water Desalination using Magnetic Flow-electrode Capacitive Deionization, *Water Res.*, 2022, **216**, 118290.
17 J. Li, W. Wei, Y. Chen and Z. Liu, Multiple Sites Organic Small-Molecule Electrode Material for High-Capacity Seawater Desalination, *ACS Sustainable Chem. Eng.*, 2024, **12**, 16388–16395.
18 Z. Chen, X. Xu, K. Wang, D. Jiang, F. Meng, T. Lu, Y. Yamauchi and L. Pan, Hybrid of pyrazine based π-conjugated organic molecule and MXene for hybrid capacitive deionization, *Sep. Purif. Technol.*, 2023, **315**, 123628.
19 P. Zhang, X. Zhang, S. Cui, L. Ke, C. Zhao and M. Shi, Ultralow-gap and structurally rigid organic molecule enables high-efficiency and long-lasting electrochemical desalination, *Chem. Eng. J.*, 2025, **522**, 167393.
20 Q. Lu, H. Duan, K. Zhang, H. Wang, D. Han, Z. Wang, Y. Xu, Q. Yi, Y. Shen, T. Yan, M. Xie and D. Zhang, Regulation of Intra-Nanopore Microenvironment in Oxygen-Rich Covalent Organic Frameworks for Enhanced Capacitive Deionization, *Adv. Funct. Mater.*, 2025, **35**, 2507253.
21 X. Gu, R. Wang, S. Yang, Y. Shangguan, X. Feng and H. Chen, Boosting Capacitive Deionization in MoS(2) via Interfacial Coordination Bonding and Intercalation-Induced Spacing Confinement, *ACS Nano*, 2025, **19**, 6488–6498.
22 G. Li, Y. Tao, T. Zhang, Y. Wu, P. Xiao, M. Guo and M. Shi, A π-conjugated imine-rich organic material with exceptional pseudocapacitive properties for high-performance electrochemical desalination, *Desalination*, 2025, **607**, 118817.
23 Z. Sahray, A. N. Shocron, R. Uwayid, C. E. Diesendruck and M. E. Suss, Extreme Monovalent Ion Selectivity Via Capacitive Ion Exchange, *Water Res.*, 2023, **246**, 120684.
24 X. Zhou, S. Shu, X. Ye and Z. Li, Engineering Faradaic Electrode Materials for High-Efficiency Water Desalination, *Small*, 2024, **20**, e2400047.

25 N. M. Aldaqqa, S. Kumar, J. I. Martinez, N. Elmerhi, E. Alhseinat and D. Shetty, Surface Engineered 2D-beta-ketoenamine Covalent Organic Framework for Superior Dechlorination via Hybrid Capacitive Deionization, *Angew. Chem., Int. Ed.*, 2025, **64**, e202510345.

26 Y. Cui, Y. Tao, J. Yang, H. Wang, P. Zhang, G. Li, M. Shi and E. H. Ang, A ladder-type organic molecule with pseudocapacitive properties enabling superior electrochemical desalination, *Mater. Horiz.*, 2025, **12**, 2341–2350.

27 L. Xiang, X. Xu, Y. Liu, H. Zhang, R. Xu, C. Li, F. Xu, Y. Yamauchi and Y. Mai, Curvature-induced ion docking effect in capacitive deionization, *Nat. Water*, 2024, **2**, 1195–1206.

28 Q. Wang, M. Zhao, Q. Wu, S. Meng, X. Li and D. Liang, Ultrahigh Salt Adsorption Capacity of Carbonaceous Electrode in a Rocking-Chair Capacitive Deionization through Surface Charge Modulation, *Environ. Sci. Technol. Lett.*, 2024, **11**, 634–639.

29 Y. Lin, H. Cui, C. Liu, R. Li, S. Wang, G. Qu, Z. Wei, Y. Yang, Y. Wang, Z. Tang, H. Li, H. Zhang, C. Zhi and H. Lv, A Covalent Organic Framework as a Long-life and High-Rate Anode Suitable for Both Aqueous Acidic and Alkaline Batteries, *Angew. Chem. Int. Ed.*, 2023, **62**, e202218745.

30 W. Zhou, T. Huang, Y. Zhao, D. Kang, C. Huang and M. Ding, Ternary-metal Prussian blue analog hollow spheres/MXene electrode based on self-assembly enabling highly stable capacitive deionization, *Chem. Eng. J.*, 2025, **508**, 161124.

31 J. Lee, H. Lim, J. Park, M. S. Kim, J. W. Jung, J. Kim and I. D. Kim, Fluorine-Rich Covalent Organic Framework to Boost Electrochemical Kinetics and Storages of K+ Ions for Potassium-Ion Battery, *Adv. Energy Mater.*, 2023, **13**, 2300442.

32 J. Peng, X. Zhao, Y. Huang, C. Zhao, J. Yang and M. Shi, Electron-Delocalized Benzimidazole-Linked Organic Electrode with Enhanced Redox Availability for High-Performance Ammonium Capture via Capacitive Deionization, *Adv. Funct. Mater.*, 2025, **35**, 2506369.

33 J. Yang, J. Peng, P. Zhang, J. Yang and M. Shi, A redox-mediated polymer with extended π-delocalization for efficient Cr^{3+} elimination via capacitive deionization, *Sep. Purif. Technol.*, 2025, **368**, 133039.

34 X. Wang, Y. Wang, Y. Jiang, X. Li, Y. Liu, H. Xiao, Y. Ma, Y. Y. Huang and G. Yuan, Tailoring Ultrahigh Energy Density and Stable Dendrite-Free Flexible Anode with Ti3C2Tx MXene Nanosheets and Hydrated Ammonium Vanadate Nanobelts for Aqueous Rocking-Chair Zinc Ion Batteries, *Adv. Funct. Mater.*, 2021, **31**, 2103210.

35 Z. Zhang, X. Xu, P. Ma, Y. Asakura, Z. Wang, Y. Yamauchi and H. Li, Pushing the limit of layered transition metal oxides with heterolattice oxygen-mediated redox for capacitive deionization, *Nat. Commun.*, 2025, **16**, 3652.

36 H. Zhang, X. Li, C. Xiao, J. Xie, X. Yan, C. Wang, Y. Zhou, J. Qi, Z. Zhu, X. Sun and J. Li, Enhanced selective electrosorption of Pb2+ from complex water on covalent organic framework-reduced graphene oxide nanocomposite, *Sep. Purif. Technol.*, 2022, **302**, 122147.

37 J. Yang, H. Fu, L. Ye, M. Shi and E. H. Ang, Tailoring surface structures in Mn-based Prussian blue analogues for enhanced NH4+ transport and high-performance aqueous batteries, *Mater. Horiz.*, 2025, **12**, 8565–8576.

38 J. Yang, X. Zhao, J. Peng, J. Yang, M. Shi, L. Zhang and C. Yan, Redox-enhanced ladder-type organic electrode enabling high-rate aqueous ammonium-ion batteries, *J. Colloid. Interface Sci.*, 2025, **700**, 138339.

39 N. Arora, F. Banat, G. Bharath and E. Alhseinat, Capacitive deionization of NaCl from saline solution using graphene/CNTs/ZnO NPs based electrodes, *J. Phys. D: Appl. Phys.*, 2019, **52**, 455304.

40 J. Lee, S. Kim, C. Kim and J. Yoon, Hybrid capacitive deionization to enhance the desalination performance of capacitive techniques, *Energy Environ. Sci.*, 2014, **7**, 3683–3689.

41 N. Chen, J. He, H. Xuan, J. Jin, K. Yu, M. Shi and C. Yan, Dual-functional Polyindole/MXene composite for superior proton storage and corrosion protection, *Composites, Part B*, 2024, **270**, 111145.

42 T. Dong, W. Yi, T. Deng, T. Qin, X. Chu, H. Yang, L. Zheng, S. J. Yoo, J. G. Kim, Z. Wang, Y. Wang, W. Zhang and W. Zheng, Diffusionless-Like Transformation Unlocks Pseudocapacitance with Bulk Utilization: Reinventing Fe2O3 in Alkaline Electrolyte, *Energy Environ. Mater.*, 2022, **6**, e12262.

43 T. Lu and F. Chen, Multiwfn: a multifunctional wavefunction analyzer, *J. Comput. Chem.*, 2012, **33**, 580–592.

44 B. Chen, A. Feng, R. Deng, K. Liu, Y. Yu and L. Song, MXene as a Cation-Selective Cathode Material for Asymmetric Capacitive Deionization, *ACS Appl. Mater. Interfaces*, 2020, **12**, 13750–13758.

45 A. G. El-Deen, N. A. M. Barakat, K. A. Khalil, M. Motlak and H. Yong Kim, Graphene/SnO2 nanocomposite as an effective electrode material for saline water desalination using capacitive deionization, *Ceram. Int.*, 2014, **40**, 14627–14634.

46 T. K. A. Nguyen, E. P. Kuncoro and R.-A. Doong, Manganese ferrite decorated N-doped polyacrylonitrile-based carbon nanofiber for the enhanced capacitive deionization, *Electrochim. Acta*, 2022, **401**, 139488.

47 M. Gao, J. Li, Z. Wang, Z. Yang, Y. Chen, W. Deng, W. Liang, T. Ao and W. Chen, Hierarchical nickel cobaltite nanoneedle arrays armored flexible electrospinning carbon nanofibers membrane for electrochemical deionization, *Sep. Purif. Technol.*, 2024, **328**, 125084.

48 M. Gao, N. Li, C. He, Y. Kang, H. Kong, L. Yang, W. Liang, T. Ao, H. Mou and W. Chen, Encapsulation hierarchical bimetallic oxide with flexible electrospinning carbon nanofibers for efficient capacitive deionization, *Desalination*, 2024, **586**, 117905.

49 Z. Wang, X. Bai, K. Zhang, H. Wang, J. Dong, Y. Gao and B. Zhao, MOF-templated synthesis of nitrogen-doped carbon for enhanced electrochemical sodium ion storage and removal, *Acta Phys. Chim. Sin.*, 2025, **41**, 100026.

50 R. Ma, W. Luo, L. Yan, C. Guo, X. Ding, X. Gong, D. Jia, M. Xu, L. Ai, N. Guo and L. Wang, Constructing the quinonyl groups and structural defects in carbon for supercapacitor and capacitive deionization applications, *J. Colloid Interface Sci.*, 2023, **645**, 685–693.

51 H. Wei, T. Wang, R. Hu, Z. Sun, I. Hussain and Y. Yang, Sulfur Vacancies Enriched Copper Sulfide Nanotubes Boost Desalination Efficiency of Hybrid Capacitive Deionization, *Small*, 2025, **21**, 2411810.

52 Y. Ren, M. Liang, Z. Zhou, X. Zhang, F. Yu, X. G. Li and J. Ma, Molecular Intercalation and Electron Modulation Stabilized 1T-MoS2 Superlattice Nanoflowers with Desolvation Regulation for Energy-Efficient Water Production, *Adv. Funct. Mater.*, 2025, **35**, 2303464.

53 S. Eris and H. Bashiri, Kinetic study of the adsorption of dyes onto activated carbon, *Prog. React. Kinet. Mech.*, 2016, **41**, 109–119.